

Multiwavelength dissection of a massive heavily dust-obscured galaxy and its blue companion at $z \sim 2$

M. Hamed¹, L. Ciesla², M. Béthermin², K. Małek^{1,2}, E. Daddi³, M. T. Sargent⁴, and R. Gobat⁵

¹ National Centre for Nuclear Research, ul. Pasteura 7, 02-093 Warszawa, Poland

² Aix Marseille Univ. CNRS, CNES, LAM, Marseille, France

³ CEA, Irfu, DAp, AIM, Université Paris-Saclay, Université de Paris, CNRS, F-91191 Gif-sur-Yvette, France

⁴ Astronomy Centre, Department of Physics and Astronomy, University of Sussex, Brighton, BN1 9QH, UK

⁵ Instituto de Física, Pontificia Universidad Católica de Valparaíso, Casilla 4059, Valparaíso, Chile

Received 02 October 2020 / Accepted 15 January 2021

ABSTRACT

Aims. In this work we study a system of two galaxies, namely Astarte and Adonis, at $z \sim 2$ when the Universe was undergoing its peak of star formation activity. Astarte is a dusty star-forming galaxy at the massive-end of the main sequence (MS) and Adonis is a less-massive, bright in ultraviolet (UV), companion galaxy with an optical spectroscopic redshift. We analyze the physical properties of this system, and probe the gas mass of Astarte with its ALMA CO emission, to investigate whether this ultra-massive galaxy is quenching or not, and whether it has always been on the MS of star-forming galaxies.

Methods. We use CIGALE - a spectral energy distribution modeling code - that relies on the energetic balance between the UV and the IR, to derive some of the key physical properties of Astarte and Adonis, mainly their star formation rates (SFRs), stellar masses, and dust luminosities. We inspect the variation of the physical parameters depending on the assumed dust attenuation law. We also estimate the molecular gas mass of Astarte from its CO emission, using different α_{CO} and transition ratios (r_{31}) and discuss the implication of the various assumptions on the gas mass derivation.

Results. We find that Astarte exhibits a MS-like star formation activity, while Adonis is undergoing a strong starburst (SB) phase. The molecular gas mass of Astarte is far below the gas fraction of typical star-forming galaxies at $z=2$. This low gas content and high SFR, result in a depletion time of 0.22 ± 0.07 Gyrs, which is slightly shorter than what is expected for a MS galaxy at this redshift. The CO luminosity relative to the total IR luminosity suggests a MS-like activity if we assume a galactic conversion factor and a low transition ratio. The SFR of Astarte is of the same order using different attenuation laws, unlike its stellar mass that increases using shallow attenuation laws ($\sim 1 \times 10^{11} M_{\odot}$ assuming a Calzetti relation versus $\sim 4 \times 10^{11} M_{\odot}$ assuming a shallow attenuation law). We discuss these properties and suggest that Astarte might be experiencing a recent decrease of star formation activity and is quenching through the MS following a SB epoch.

Key words. galaxies: evolution - galaxies: high-redshift - galaxies: star formation - galaxies: starburst - infrared: galaxies - ISM: dust, extinction.

1. Introduction

Studying galaxy evolution throughout the cosmic time is a key element of modern astrophysics, and is crucial for our understanding of the life cycle of the progenitors of passive elliptical galaxies that we observe in the local Universe. Evidences suggest that the star formation rate (SFR) density has peaked around a redshift of $z \approx 2$ (e.g., Hopkins & Beacom 2006; Madau & Dickinson 2014; Béthermin et al. 2017; Gruppioni et al. 2020), making this epoch (the cosmic noon) particularly interesting. Moreover, the cosmic noon epoch is when the dusty star-forming galaxies (DSFGs) (e.g., Smail et al. 1997; Blain et al. 2002; Weiß et al. 2013a; Casey et al. 2014; Donevski et al. 2020) contributed significantly to the star formation activity of the Universe (e.g., Chapman et al. 2003, 2005). Furthermore, the dust-obscured star formation activity plays an important role at higher redshifts (e.g., Takeuchi et al. 2005; Murphy et al. 2011; Béthermin et al. 2015; Bourne et al. 2017; Whitaker et al. 2017). It is therefore crucial to study the massive DSFGs at higher redshift.

The affluence of multiwavelength data, especially the far infrared (FIR) detections from *Herschel*, played a central role in understanding how DSFGs evolve as a function of redshift.

However, there are still controversies regarding how these galaxies build up their stellar masses. These controversies arise from the systematic uncertainties caused by the heavy dust attenuation in this type of objects (e.g., Hainline et al. 2011; Michałowski et al. 2012). This is caused by the sensitivity of the stellar mass estimate to the type of star formation history (SFH), the choice of the synthetic stellar population (SSP), and the assumed initial mass function (IMF). The debate about the accuracy of derived stellar masses of DSFGs was also discussed in details in Casey et al. (2014).

On the other hand, the growing number of ALMA observations in the recent years is providing an unparalleled help in constraining the evolution of DSFGs. These data are allowing us to build a comprehensive view of the role of these giant IR-bright sources by tracing their molecular gas and dust content (e.g., Donevski et al. 2020). The wealth of multiwavelength data also contributed to improve significantly estimating physical properties that govern such galaxies, by modeling their spectral energy distribution (SED, e.g., Burgarella et al. 2005; da Cunha et al. 2008; Noll et al. 2009; Conroy 2013; Ciesla et al. 2014).

To build an SED, different aspects of a galaxy must be considered, most importantly the star formation history (SFH), the change of which has a strong impact on the derived SFR (e.g. Buat et al. 2014; Ciesla et al. 2017), stellar populations of varied ages and metallicities, dust emission with different dust grain sizes and temperatures, nebular and synchrotron emissions, etc. Extinction caused by dust is critically important in any spectrum fitting of a galaxy, since it mutates the shape of the SED the most by absorbing a significant amount of the UV photons and thermally re-emitting them in the IR. This behavior can be modeled by assuming that dust absorbs the shorter wavelength spectrum of galaxies following attenuation laws, which are typically described by simple power laws with varying complexities, and is able to reproduce the observed extinction in galaxies of different redshifts and types. However, dust attenuation laws are not universal (e.g., Wild et al. 2011; Buat et al. 2018; Małek et al. 2018; Salim & Narayanan 2020). The need of different attenuation recipes is inevitable in order to reproduce the spectra of galaxies of different masses, IR luminosities and naturally the redshift. This makes it challenging to interpret some of the physical features especially when different attenuation laws can reproduce a good SED of a galaxy Buat et al. (2019).

A non-negligent fraction of galaxies exhibit a non-alignment and sometimes a total disconnection between the dust continuum and the stellar population (Dunlop et al. 2017; Elbaz et al. 2018). This directly challenges SED fitting techniques that rely on the energetic balance between the UV and the IR, since the key assumption for such techniques is that any physical property derived from one part of the spectrum should be valid for the entire galaxy. Several approaches were investigated to test the validity of this strategy, Buat et al. (2019) suggested the decoupling of the stellar continuum from the IR emission by modeling their fluxes apart to compare the derived parameters such as the SFRs, dust luminosities and stellar masses with the ones derived using full SEDs. Statistical samples of such massive and dusty galaxies (e.g., Dunlop et al. 2017; Elbaz et al. 2018; Buat et al. 2019; Donevski et al. 2020) offer an important insight into the evolution of dust and gas mass through the cosmic time. However, the nature of these giants is not fully understood.

The interstellar medium (ISM) is the most important element in understanding the physical processes of star formation itself, since it contains the building materials for future stars, most importantly the hydrogen. Hydrogen's density was found to be tightly correlated with the SFR, as suggested by Schmidt (1959) and investigated by Kennicutt (1998). This correlation is known as the Schmidt-Kennicutt law, and it takes into account the gas in its molecular and atomic forms, albeit the molecular gas having the biggest impact. The mass of this gas can be estimated with the emission of the easily excited CO molecules (e.g., Carilli & Walter 2013; Weiß et al. 2013b; Decarli et al. 2019; Riechers et al. 2020). Tracing the molecular gas with CO emission relies entirely on already established abundances in galaxies of the local Universe. Large interferometers such as ALMA offer unique opportunities to detect these emission lines with an unprecedented accuracy, the luminosity of which can give an estimate of the molecular hydrogen mass of a galaxy, typically using a conversion factor. On the other hand, conversion factors in high-redshift galaxies are highly debated (see Bolatto et al. 2013 for a comprehensive review).

Nonetheless, an estimate of the molecular gas reservoir of galaxies at the high-mass end of the main sequence is crucial to characterise their star formation activity. For instance, Elbaz

et al. (2018) showed that some galaxies exhibit a SB-like gas depletion time scale despite residing on the MS.

Despite the growing number of detection of such heavily dust-obscured ultra-massive objects at high redshift, the progress of SED modeling, and the better comprehension of the high-redshift ISM, we still lack a full picture of how these galaxies form and quench. Were they always steadily forming stars along the MS? Or are they former SBs transiting to the red sequence through the main sequence?

To answer these questions, it is essential to understand how is the star formation fueled by the gas in massive objects, and why does this activity cease. Quenching mechanisms are still not fully understood and they might be caused by AGN feedback or outflows (e.g. Cattaneo et al. 2009; Dubois et al. 2013; Combes 2017) to environmental effects that can lead to gas stripping (e.g. Coil et al. 2008; Mendez et al. 2011).

In this paper, and motivated by the aforementioned questions, we analyze and interpret the multi-wavelengths observations of a pair of galaxies at $z \sim 2$, with original COSMOS2015 catalog Laigle et al. (2016) IDs: 647980 and 648299, hereafter Astarte and Adonis. Astarte is an ultra-massive ($M_{\star} > 10^{11} M_{\odot}$), IR-bright galaxy, for which the CO emission is serendipitously detected with ALMA. Adonis is a low-mass galaxy bright in near-UV (NUV) and optical bands.

The structure of this paper is as follows: in Section 2 we describe the data of the two galaxies analysed in this work. In Section 3.1 we probe the molecular gas of Astarte using its ALMA-detected CO emission line, and in Section 3.1.5 we investigate the morphology of this line compared to multiwavelength detection. In Section 3.2 we derive the physical properties of the two galaxies using SED fitting. The discussion and the conclusion are in Sections 4 and 5 respectively.

Throughout this paper, we adopt the stellar initial mass function (IMF) of Chabrier (2003) and a Λ CDM cosmology parameters (WMAP7, Komatsu et al. 2011): $H_0 = 70.4 \text{ km s}^{-1} \text{ Mpc}^{-1}$, $\Omega_M = 0.272$, and $\Omega_{\Lambda} = 0.728$.

2. Observations

The system of Astarte and Adonis studied in this paper was initially part of a selection of $z \sim 2$ galaxies at the high-mass end ($M_{\star} > 10^{11} M_{\odot}$) of the main-sequence (MS) of star-forming galaxies (e.g., Noeske et al. 2007; Daddi et al. 2010; Rodighiero et al. 2011; Schreiber et al. 2015) detected by *Herschel*/PACS observations of the COSMOS field (PEP survey, Lutz et al. 2011). In the COSMOS2011 catalog where the system was selected, the system is not deblended even in the optical and near-IR and appears as a single source. It is probably caused by the fact that this early catalog is mainly built using the *i* band, where Astarte is particularly faint. The zCOSMOS survey Lilly et al. (2009) measured the spectroscopic redshift at the position of the HST/ACS source from zCOSMOS and found $z_{spec} = 2.140$. In the more recent COSMOS catalog Laigle et al. (2016), both *z* and near-infrared bands were used to detect and deblend the object. Adonis and Astarte have thus an individual measurements of their flux in the optical bands of Subaru, the NIR bands of VISTA, and the mid-IR with *Spitzer*/IRAC. Astarte is detected at 250 and 350 μm with *Herschel*/SPIRE using a 24 μm prior Oliver et al. (2012). The aforementioned deblending, coupled with the FIR detection of Astarte results in a low-mass low-SFR object ($\text{SFR} = 37 M_{\odot} \text{ yr}^{-1}$ with a stellar mass of $9.46 \times 10^9 M_{\odot}$), and a dust-obscured ultra-massive object ($\text{SFR} = 131 M_{\odot} \text{ yr}^{-1}$

with a stellar mass of $1.41 \times 10^{11} M_{\odot}$, as estimated initially using LePhare [Arnouts & Ilbert \(2011\)](#).

Astarte and Adonis were observed by ALMA as part of a program (2013.1.00914.S, PI: Bethermin) targeting a pilot sample of four massive $z \sim 2$ main-sequence galaxies in band-7 continuum and their CO emission. The goal was to measure their gas and dust content and to compare their short-wavelength morphology with their CO and continuum morphologies.

2.1. NUV-IR observations

The NUV (rest-frame FUV) detections of our two galaxies are provided by the Canada France Hawaii Telescope (CFHT) in the u band. Visible and NIR detections (rest-frame mid-UV to NUV) are obtained via the broad band Suprime-Cam of Subaru in the B , V , r , i^+ bands and the mid-IR data (rest-frame NIR) are from the IRAC camera of *Spitzer*. The IR-bright Astarte has a MIPS detection at $24 \mu\text{m}$ with a signal-to-noise ratio (hereafter S/N) > 20 and is very bright (S/N ~ 20) in IR detections of *Herschel* where the beam size is large. The $100 \mu\text{m}$ observation from PACS does not detect any of the two galaxies, but provides an upper limit, which is taken into account by the SED fitting of Astarte since it constrains the far-IR part of the spectrum.

The radio continuum of Astarte is tentatively detected with the Karl G. Jansky Very Large Array (VLA) in the S band at $\nu = 3 \text{ GHz}$ [Smolčić et al. \(2017\)](#). This tentative detection was not included in the initial catalog of [Smolčić et al. \(2017\)](#), since it falls just below their detection threshold of 5σ (S/N=4.3). Adonis does not have any detection from VLA at 3 GHz. We thus estimated a 3σ upper limit from the standard deviation in the cutout image around our two sources. The beam width of the VLA detection is $0.75''$, and the continuum is shown in Figure 1.

The [Jin et al. \(2018\)](#) catalog provides JCMT's fluxes at $850 \mu\text{m}$ for both of our galaxies ($2440 \pm 2519 \mu\text{Jy}$ for Astarte and $3910 \pm 2516 \mu\text{Jy}$ for Adonis). We refrain from using these super-deblended fluxes due to the high uncertainties, probably caused by the degeneracies in the deblending of such a close pair, and since the majority of flux is unexpectedly attributed to the smaller less IR-bright Adonis. Table 1 presents a summary of the available photometric data from different instruments of the two galaxies.

2.2. ALMA observation

Astarte was observed at 2.7 mm with ALMA (band 3) with a time-on-source of 45 minutes using 32 antennas on September the 5th of 2015, cycle-2 (P.I. M.Bethermin). We use the Common Astronomy Software Applications package and pipeline (CASA) v5.4¹ ([McMullin et al. 2007](#)) for flagging and to reduce the visibility data. The deconvolution was performed with the CLEAN algorithm using natural weighting for an optimal S/N. Multi-frequency synthesis mode of the line-free channels showed a non-significant continuum emission of the spectrum therefore its subtraction was not needed. In the deconvolution process, the cell size was set to $0.1''$. The achieved synthesized beam size is $0.78'' \times 0.56''$, the velocity resolution of the cube is 21.36 km s^{-1} and the rms is $0.47 \text{ mJy beam}^{-1} \text{ km s}^{-1}$ per channel.

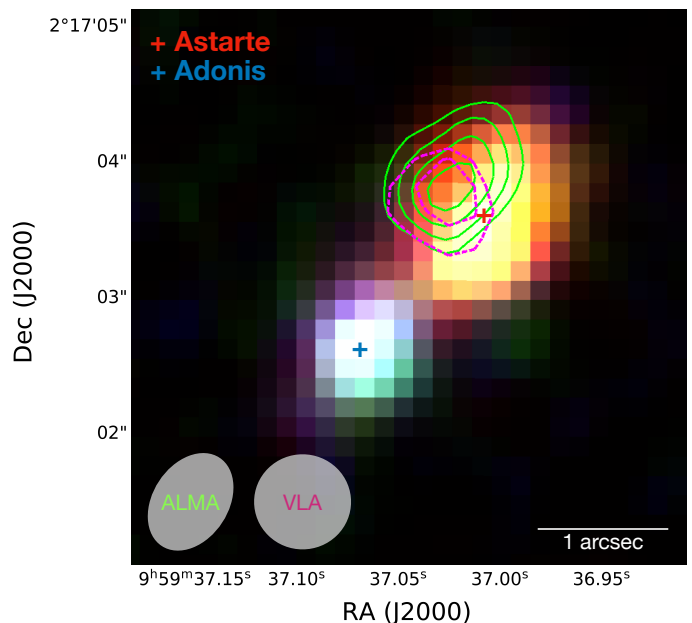


Fig. 1. Integrated flux of ALMA-detected CO emission (green contours), along with the VLA-detected radio continuum at 3 GHz (magenta contours), on the RGB image (VISTA's Ks, H and J) of Astarte and Adonis. The beam size of ALMA is $0.78'' \times 0.50''$ (lower left beam). The beam FWHM of VLA is $0.75''$. The outermost contour of the CO integrated flux (green) is at 2σ significance. The subsequent contours are in steps of 1σ with the innermost contour showing 5σ . The magenta contours show 2 and 3σ significance. The blue cross is centered on Adonis, the red cross is centered on Astarte.

		Astarte	Adonis	
COSMOS15 ID		647980	648299	
redshift		$z_{\text{phot}} = 2.153$	$z_{\text{spec}} = 2.140$	
Telescope/ Instrument	Filter	λ (μm)	S_{ν} (μJy)	
CFHT/ MegaCam	u	0.383	0.104 ± 0.032	0.492 ± 0.032
Subaru/ Suprime-Cam	B	0.446	0.127 ± 0.018	0.596 ± 0.032
	V	0.548	0.252 ± 0.033	0.938 ± 0.049
	r	0.629	0.246 ± 0.029	0.904 ± 0.041
	i^+	0.768	0.331 ± 0.035	0.973 ± 0.042
	z^{++}	0.910	0.719 ± 0.062	1.329 ± 0.063
VISTA/ VIRCam	Y	1.02	0.836 ± 0.155	1.519 ± 0.162
	J	1.25	2.691 ± 0.175	2.682 ± 0.181
	H	1.65	4.234 ± 0.241	3.243 ± 0.254
	Ks	2.15	9.536 ± 0.351	4.776 ± 0.362
<i>Spitzer</i>	IRAC1	3.6	18.60 ± 0.07	3.70 ± 0.10
	IRAC2	4.5	25.10 ± 0.10	2.80 ± 0.13
	IRAC3	5.8	25.10 ± 2.00	3.60 ± 2.60
	IRAC4	8.0	15.30 ± 3.30	-
<i>Spitzer</i>	MIPS1	24	351 ± 17	
<i>Herschel</i>	PACS	100	< 6734	
<i>Herschel</i>	SPIRE	250	17792 ± 744	-
	SPIRE	350	16058 ± 1026	-
ALMA	band 3	3100	< 117	
VLA	S	1.3×10^5	9.9 ± 2.3	< 7.3

Table 1. Summary of the data of the two sources observed through the different instruments. S_{ν} is the flux in (μJy). λ is the center of the specific filter band.

¹ <https://casa.nrao.edu/>

3. Results

3.1. Probing the molecular gas of Astarte

In the data cube we find only one significant line and no significant continuum source in the field of view. The line extraction procedure along with the derivation of the luminosity and the gas mass are described in the following subsections.

3.1.1. Line extraction

The ALMA-detected emission line of Astarte corresponds to the CO(3-2), with a peak at an observed frequency of $\nu_{obs} = 109.65$ GHz implying $z_{CO(3-2)} = 2.154$, which agrees with the photometric redshift $z_{phot,Astarte} = 2.153^{+0.051}_{-0.058}$ Laigle et al. (2016). This validates Astarte as the origin of the detected-CO emission. We do not detect Astarte in the continuum and measured a $3\text{-}\sigma$ upper limit from the map of 0.117 mJy. The expected flux densities from the SED modeling discussed in Sect.3.2.6 are 0.007 mJy and 0.049 mJy for Adonis and Astarte, respectively. It is thus not surprising that none of our two sources are detected. The flux uncertainty was determined by deriving the standard deviation in the source-free pixels in the non primary-beam corrected map, since it has similar noise levels across the emission-free pixels (the noise at the central region is $\sim 2\%$ higher than the outermost region of the map). The achieved S/N is 5.2 for the brightest channel of the CO(3-2) of Astarte. The emission line was extracted by fitting a Gaussian over the profile. The goodness of the Gaussian fit was verified with a χ^2 test, its properties are summarized in Figure 2 along with the redshifted CO(3-2) line. The full width at half maximum (FWHM) of the Gaussian is found to be $152.74 \pm 33.21 \text{ km s}^{-1}$. The spectroscopic redshift

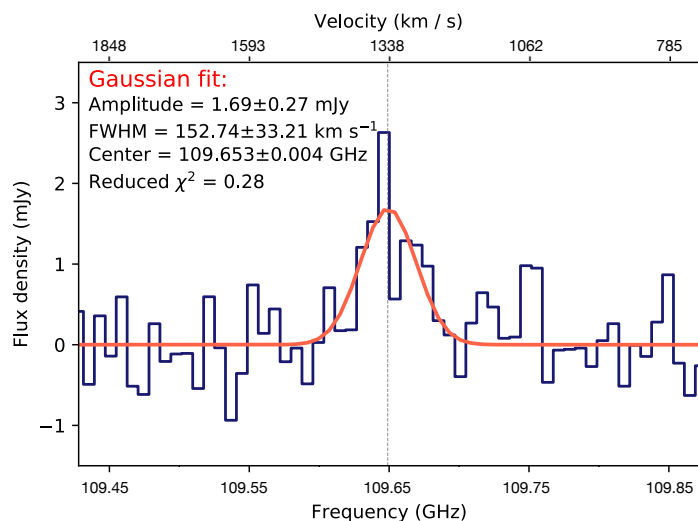


Fig. 2. Spectral profile of Astarte with the redshifted CO(3→2) line (dashed vertical grey line) and the Gaussian fit (red) with its properties.

of the system at the position of HST detection found by the zCOSMOS survey Lilly et al. (2009) is $z_{spec} = 2.140$. This z_{spec} corresponds to that of Adonis since only this UV-bright galaxy is detected with HST/ACS. Taking into account the redshift difference of Astarte and Adonis, the corresponding radial velocity difference ΔV is 1335 km s^{-1} . This velocity difference is greater than what is found in interacting pairs of galaxies, which is typically $\Delta V < 350 \text{ km s}^{-1}$ (Lambas et al. 2003; Alonso et al. 2004). Outflows and absorption in the UV lines could account for few hundreds of km s^{-1} Cassata et al. (2020), or a division of the

Hubble flow and peculiar motions, which could account for a significant velocity contribution if it is along the line of sight. Therefore, this does not eliminate a possible interaction between Astarte and Adonis.

3.1.2. Line integrated flux and luminosity

The intensity is calculated by integrating over the Gaussian fit of the line, which is then converted to the apparent line luminosity (L'), by using the expression from Solomon et al. (1997) that expresses L' with the integrated source brightness temperature in units of $K \text{ km s}^{-1} \text{ pc}^2$:

$$L'_{line} = 3.25 \times 10^7 \times I \times \frac{D_L^2}{(1+z)^3 \nu_{obs}^2},$$

where D_L is the luminosity distance in (Mpc), I is the intensity in (Jy km/s), and ν_{obs} is the observed frequency in (GHz). As a consistency test, we also estimated the integrated flux of the line using the moment-zero map, which was obtained by summing the channels where the emission line is detected. The line flux is measured in the moment-0 map using a 2-dimension Gaussian fit of the source. As shown in Béthermin et al. (2020), there is no significant difference between this method and a fit in the uv plane for faint compact sources observed by ALMA. The resulting flux densities of the two methods are presented in Table 2. There is 1.2σ significant difference between the intensities derived by each methods. The spectrum is extracted at a single point assuming a point source, while the 2-dimension fit can recover the flux from an extended source. This small difference of flux suggests that our source could be marginally resolved. Hereafter, we use the flux from the moment-0 map, which takes this account. However, we cannot formally exclude another faint and diffuse component at larger scale considering the depth of our data. Figure 1 shows the flux-integrated moment-0 map of Astarte represented by confidence levels contours. The size of the CO disk is $\sim 74 \text{ kpc}$.

Peak flux density (mJy)	$I_{CO(3-2)}^{spec}$ (Jy km s ⁻¹)	$I_{CO(3-2)}^{mom}$	$L'_{CO(3-2)}$ (10 ⁹ K km s ⁻¹ pc ²)
1.690 ± 0.277	0.251 ± 0.062	0.328 ± 0.047	8.508 ± 1.219

Table 2. Summary of the CO(3-2) emission line properties of Astarte. $I_{CO(3-2)}^{spec}$ is achieved by integrating over the Gaussian of the emission line. $I_{CO(3-2)}^{mom}$ is the intensity derived from the moment-0 map.

3.1.3. Deriving the molecular gas mass

To derive the total mass of the molecular gas in a galaxy we assume that the H_2 mass is proportional to the CO(1-0) line luminosity which is the commonly used tracer of the cold star-forming molecular clouds, thanks to its small excitation potential requirement. The H_2 mass can be derived using a conversion factor α_{CO} (e.g. Downes & Solomon 2003; Greve et al. 2005; Tacconi et al. 2006; Carilli & Walter 2013; Bothwell et al. 2013b):

$$M_{H_2} = \alpha_{CO} L'_{CO(1-0)}$$

where M_{H_2} is the mass of the molecular hydrogen in M_\odot , α_{CO} is the conversion factor and $L'_{CO(1-0)}$ is the line luminosity in $K \text{ km s}^{-1} \text{ pc}^2$. The practice of H_2 mass derivation with this method is very common especially for galaxies at high redshifts

where information and spatial resolution is often limited. Our CO(3-2) line luminosity has to be converted to CO(1-0) luminosity using a luminosity line ratio $r_{31} = L'_{CO(3-2)}/L'_{CO(1-0)}$. We use $r_{31} = 0.42 \pm 0.07$, which is the average ratio found for $z = 1.5$ SFGs by [Daddi et al. 2015](#). This results in:

$$L'_{CO(1-0)} = (2.03 \pm 0.59) \times 10^{10} K km s^{-1} pc^2.$$

To convert this luminosity into hydrogen mass, we use two conversion factors: $\alpha_{CO} = 0.8$ and a galactic conversion factor of $\alpha_{CO} = 4.36$. The first one manages to recover the molecular gas mass in starbursts (SBs) and submillimeter galaxies (SMGs), where the gas is efficiently heated by dust. The galactic conversion factor is suitable for normal main sequence galaxies ([Downes & Solomon 1998](#); [Bolatto et al. 2013](#); [Carilli & Walter 2013](#)). For $\alpha_{CO} = 0.8$, the mass of the molecular hydrogen is:

$$M_{H_2(\alpha=0.8)} = (1.62 \pm 0.47) \times 10^{10} M_{\odot}.$$

Whereas $\alpha_{CO} = 4.36$ results in $M_{H_2} = (8.85 \pm 2.57) \times 10^{10} M_{\odot}$, five times larger gas reservoir than the one derived with $\alpha_{CO} = 0.8$.

3.1.4. Dynamical mass

With the velocity FWHM of the CO(3-2) line, we use the method described in [Bothwell et al. \(2013a\)](#) to estimate the dynamical mass of Astarte. Assuming that a rotating disk is the origin of the detected line, the dynamical mass can be written as in [Neri et al. \(2003\)](#):

$$M_{dyn} (M_{\odot}) = 4 \times 10^4 \Delta V^2 R / \sin^2(i),$$

where ΔV is the FWHM of the line velocity, i is the inclination angle of the disk and R is the radius of the disk in kpc. For a random inclination of $\langle i \rangle = 57.3^\circ$ ([Law et al. 2009](#)), the dynamical mass is found to be $(1.11 \pm 0.23) \times 10^{11} M_{\odot}$.

The gas mass to dynamical mass ratio for a galactic conversion factor is therefore $M_{H_2}/M_{dyn} = 0.76 \pm 0.33$. For $\alpha_{CO} = 0.8$, $M_{H_2}/M_{dyn} = 0.15 \pm 0.07$.

The hydrogen mass derived assuming a galactic conversion factor is able to trace the dynamical mass of Astarte, despite the relatively low FWHM of the CO line, as it is for similar FWHM values in [Bothwell et al. \(2013b\)](#).

3.1.5. CO emission morphology

We investigate the morphology of the CO(3-2) emission line of Astarte in relation to other wavelength detections of the system, to closely study the association of the CO component with the UV, optical and IR components, as shown in [Figure 3](#).

HST's observation in the I band (mid-UV rest-frame) do not show Astarte due to its heavy dust obscuration. However, the young stellar population of the less-dusty Adonis is visible in HST's I band and is bright in the u band detection of CFHT (rest-frame far-UV) and in the J band of VISTA (rest-frame NUV). In the Ks bands of CFHT and VISTA, which correspond to rest-frame visible light, Adonis becomes less-bright, and is very faint at higher wavelengths observations of ALMA and VLA.

The dusty Astarte is not visible in the u band of CFHT (rest-frame FUV). It is however detected in the Ks bands of VISTA and CFHT showing a bright stellar population in the visible rest-frame wavelengths. A spatial offset (of $\sim 0.39''$) is visible between the ALMA-detected CO emission and the emission of

the stellar population (observed in the Ks bands) of Astarte. [Faisst et al. \(2020\)](#) found an average offset between the COSMOS2015 catalogue and the Gaia reference frame of $\Delta(RA) = -63.9^{+70.7}_{-60.2}$ milliarcsec and $\Delta(Dec) = -1.4^{+80.4}_{-67.3}$ milliarcsec. This systematic offset cannot explain the visible offset between the CO emission and the rest-frame optical counterparts of Astarte. Moreover, we show that the continuum detected by the VLA at 3 GHz of Astarte and its CO emission detected by ALMA are aligned, eliminating the possibility of a systematic error due to ALMA's synthesized beam size.

Although the original spectroscopic redshift of 2.140 (for both sources) found by zCOSMOS ([Lilly et al. 2009](#)), was derived from the visible range of HST's observation, where Astarte is not observed, ALMA offers a spectroscopic redshift for the latter ($z_{ALMA} = 2.154$). This shows the importance of long-wavelengths detections especially for dust-obscured galaxies where the UV-NIR emission is heavily attenuated ([Schreiber et al. 2018b](#); [Wang et al. 2019](#)).

3.2. SFRs, stellar masses and dust luminosities

3.2.1. The SED modeling

We use the SED modeling code CIGALE² ([Boquien et al. 2019](#)) to derive the physical properties of our sources. The code allows to model galaxies' SED from the UV to the radio wavelengths, taking into account the energetic balance between the emission absorbed by dust in the UV-visible range and the IR emission. CIGALE offers a variety of modules for each physical process a galaxy may undergo. The modules that we use in our SED fitting procedures are described below.

3.2.2. Stellar component

To model the stellar component of Astarte and Adonis, we use the stellar population synthesis of [Bruzual & Charlot \(2003\)](#). This stellar library computes the direct stellar contribution to the spectrum (UV-NIR range) by populating the galaxy with young and old stars of different masses, as well as the required gas mass that will produce such population. This model was developed based on observations of nearby stellar populations and it describes well the various stellar emissions that one expects to encounter in any galaxy. These models depend on the metallicity and the separation age³. We use a solar-like metallicity and we take into account nebular emission since they contribute to the total SED model from the UV to NIR.

Different stellar demographics must be modeled with an appropriate SFH in any SED modeling, since it is critical to estimate the contribution of the young and old stars to the total flux. An appropriate SFH is key to derive the SFR of a galaxy as it strongly depends on the assumptions made ([Ciesla et al. 2017](#)). CIGALE offers different SFH scenarios varying from the simple delayed SFH to more complex ones containing episodes of bursts or sudden drops in SFRs. We use the SFH proposed by [Ciesla et al. \(2017\)](#) which is a combination of a smooth delayed buildup of the stellar population to model the long term SFH of a galaxy, and a recent flexibility in the last few hundred Myrs to allow for recent and drastic SFR variations (burst or quench). This SFH model has been proven to limit biases by decoupling the estimations of the stellar mass, mainly constrained by rest

² <http://cigale.lam.fr>

³ Age of the separation between the young stellar population and the old one.

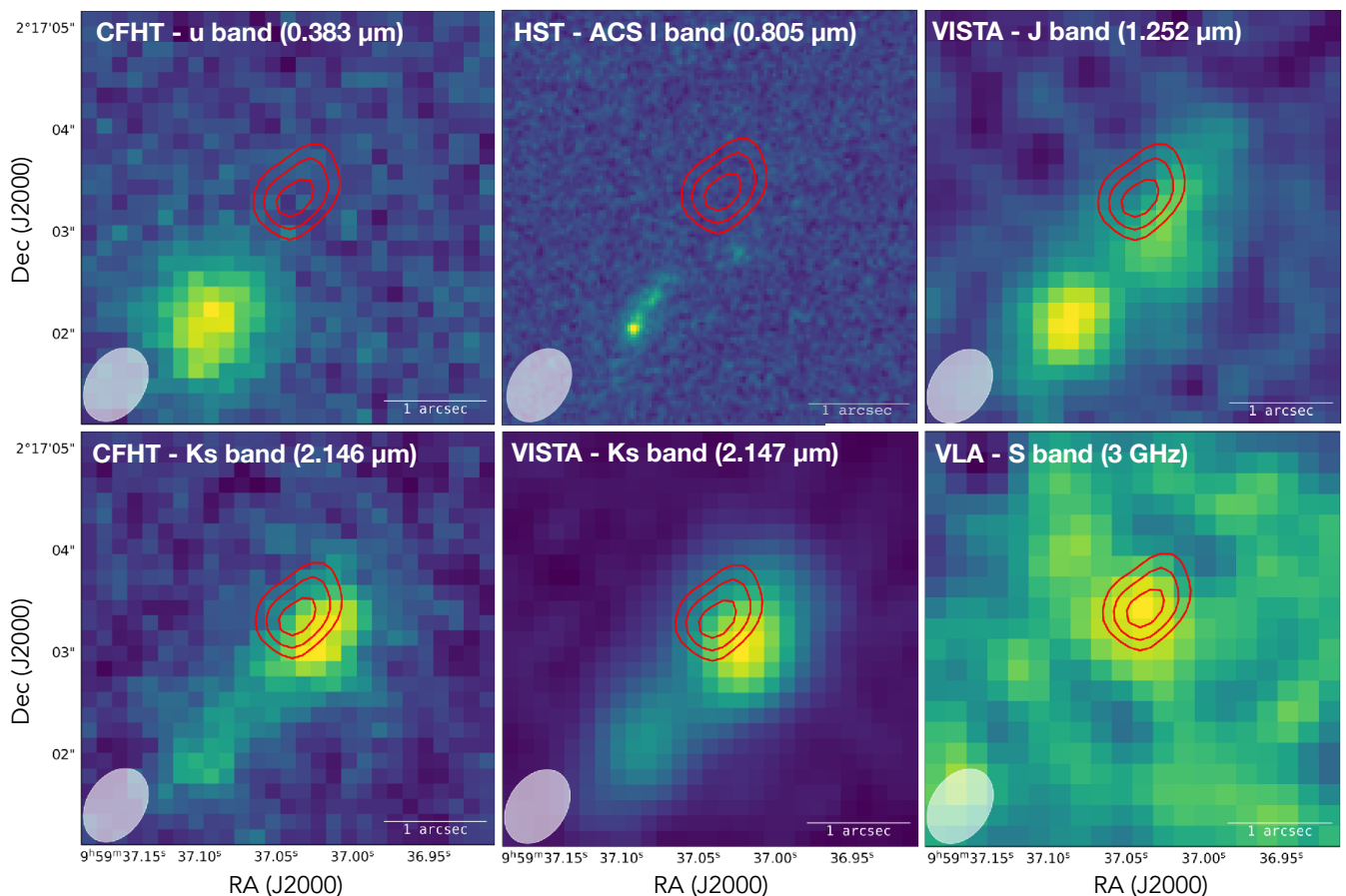


Fig. 3. ALMA-detected CO(3-2) emission line contour map (red contours) of Astarte overlaid on detections from different telescopes/instruments at different bands as specified in every figure. From upper left to lower right: CFHT U band at $0.383 \mu\text{m}$. HST's I band at $0.805 \mu\text{m}$. VISTA J band at $1.252 \mu\text{m}$. CFHT Ks band at $2.146 \mu\text{m}$. VISTA Ks band at $2.147 \mu\text{m}$ and on the VLA detection at 3GHz. The outermost contour is 3σ , and the subsequent contours are in steps of 1σ with red innermost contour showing 5σ . The beam size is $0.78'' \times 0.50''$. The white bar shows 1 arcsecond scale.

frame NIR data, from the SFR, constrained by UV and IR data (e.g., Ciesla et al. 2016, 2018; Schreiber et al. 2018a,b). This kind of SFH was used in the study of high-redshift ($z < 3$) passive galaxies to model their SED (e.g., Schreiber et al. 2018a,b; Merlin et al. 2018). We limit the recent burst/quench episodes to the last 100 Myrs of the life of our sources. The recent burst is motivated by the ALMA detection, however, it is important to note that this burst makes it difficult to constrain the past SFH. The burst part of the SFH is usually responsible for fitting the UV data, whereas the previous SFH (delayed) is driven by for the older stellar population, manifested in the visible part of the SED.

3.2.3. Attenuation laws

Two prominent attenuation laws are the ones of Calzetti et al. (2000) (hereafter C00) and Charlot & Fall (2000) (hereafter CF00). They are widely used in the literature, and along with their alternations can describe the behavior of the extinction in the UV to NIR caused by dust.

C00 and its recipes is in its core equivalent to reducing the short-wavelength flux coming from a stellar population by an opaque screen, with the opacity being dependant on the total extinction of the stellar emission at the B and V bands.

Another approach is CF00 power-law which is fundamentally different from C00: it attributes different attenuation to the ISM

and to the birth clouds (hereafter BC). This makes the dust more effective at absorbing the UV light since the young stellar emission has to pass through the dust in the BC and the ISM. Stars that are older are attenuated only by the ISM dust. The CF00 approach is slightly more complex and physical than C00 for high redshift ultra dusty galaxies, embodying different dust distributions and densities throughout a galaxy.

C00 and CF00 rely for their efficiency of attenuating the stellar population on power-laws for their slopes. The power-law slopes for BCs and ISM in CF00 were originally fixed at -0.7 each. Lo Faro et al. (2017)'s recipe (hereafter LF17) of CF00 was tuned by assuming a power-law for the slope of the attenuation in the ISM equal to -0.48. This recipe provides a steeper attenuation curve at shorter wavelengths. In this work we use these three attenuation laws and compare their best fits and their effects on deriving the physical properties of our sources.

To assess which attenuation laws to use when different modules can produce good and comparable fits, we employ the Bayesian information criterion (BIC), defined as $\chi^2 + k \ln n$, where χ^2 is the non reduced goodness of the fit, k is the degrees of freedom of the model and n is the total number of photometric fluxes used in the fit of the galaxy. We then evaluate the preference of a model over the other one by calculating the difference between their BICs: $\Delta BIC > 2$ translates into a notable difference between the two laws and the fit with the lowest χ^2 is preferred. This method was used by Ciesla et al. (2018) for

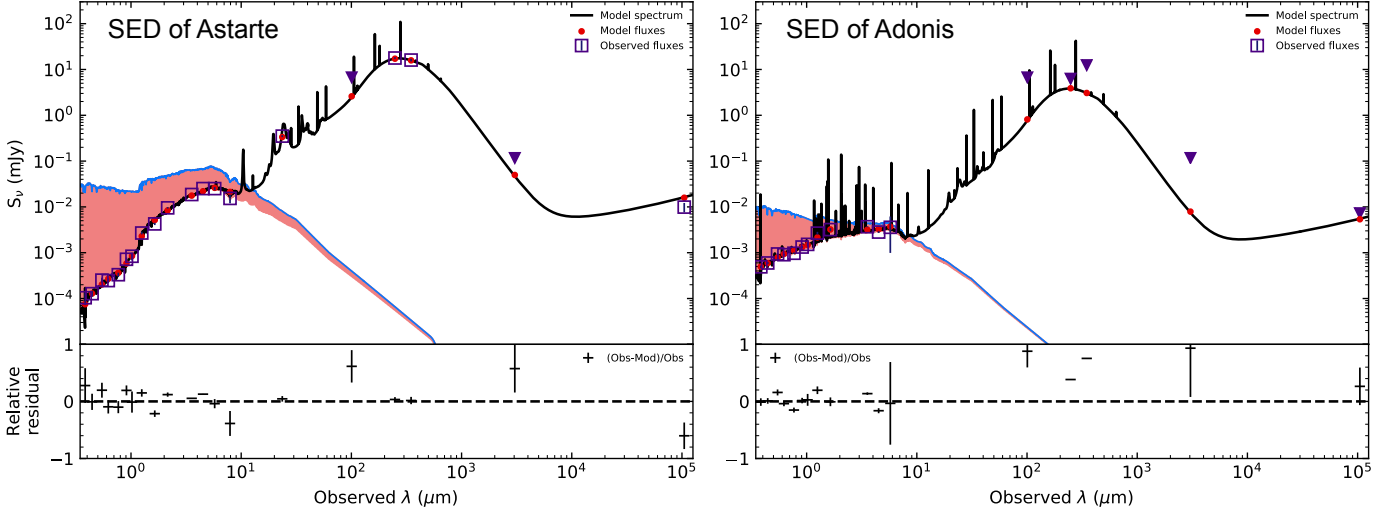


Fig. 4. Best fits of the constructed SEDs of Astarte and Adonis along with their relative residuals. The SED of Astarte (left) is produced using LF17 attenuation law. The SED of Adonis (right) is produced using CF00 attenuation law. The best fit is shown in black. The unattenuated stellar emission is shown with the blue line. The filled region shows the difference between the unattenuated and the attenuated stellar emission, absorbed by dust. Red dots are the best fit values of the observations which are shown with the purple boxes. Upper limits are shown as purple triangles.

Parameter	Values	
Star formation history (Ciesla et al. (2017))		
Stellar age ⁽ⁱ⁾	age_{main}	0.8 - 3.2 Gyr by a bin of 0.2 Gyr
e-folding time ⁽ⁱⁱ⁾	τ_{main}	0.8, 1, 3, 5, 8 Gyr
Age of burst/quench episode	t_{flex}	5, 10, 50, 100 Myr
SFR ratio after/before	r_{SFR}	$10^{-2}, 10^{-1}, 0, 10^1, 10^2, 10^3$
Stellar synthesis population (Bruzual & Charlot 2003)		
Initial mass function	IMF	(Chabrier 2003)
Metallicity	Z	0.02
Separation age		10 Myr
Dust attenuation laws (Calzetti et al. 2000)		
Colour excess of young stars	$E(B-V)$	0.1 - 1 by a bin of 0.1
Reduction factor ⁽ⁱⁱⁱ⁾	f_{att}	0.3, 0.5, 0.8, 1.0
(Charlot & Fall 2000), (Lo Faro et al. 2017)		
V-band attenuation in the ISM	A_V^{ISM}	0.3 - 3 by a bin of 0.1
$A_V^{ISM} / (A_V^{BC} + A_V^{ISM})$	μ	0.3, 0.5, 0.8, 1
Power law slope of the ISM		-0.7, -0.48
Power law slope of the BC		-0.7
Dust emission model (Draine et al. 2014)		
Mass fraction of PAH	q_{PAH}	1.77, 2.50, 3.19
Minimum radiation field	U_{min}	10, 25, 30, 40
Power law slope	α	2
Synchrotron emission		
FIR/radio correlation coefficient		2.3 - 2.9 by a bin of 0.1
Power law slope	$\alpha_{synchrotron}$	0.4 - 0.9 by a bin of 0.1

Table 3. Input parameters used to fit the SEDs of Astarte and Adonis with CIGALE. (i) The stellar age is the age of the main stellar population. (ii) The e-folding time is the time required for the assembly of the majority of the stellar population. (iii) The reduction factor f_{att} is the color excess in old stars relative to the young ones.

carefully choosing successful scenarios of SFHs of quenching galaxies, and by Buat et al. (2019) for assessing SEDs of $z \sim 2$ ALMA-detected galaxies.

3.2.4. Dust emission

To model the dust emission we use the Draine et al. (2014) IR emission models, which was calibrated using high resolution observation of the Andromeda galaxy. Draine et al. (2014) considers a variety of dust grains heated by different intensities coming from the stars and the photodissociation regions, and is an im-

	Attenuation law	χ^2	reduced χ^2	BIC
Astarte	C00	43.22	2.12	73.18
	CF00	18.34	0.97	51.30
	LF17	16.06	0.84	49.01
Adonis	C00	16.28	1.10	46.78
	CF00	10.51	0.70	41.01
	LF17	13.99	0.93	44.49

Table 4. Comparison between the quality of fits of Astarte and Adonis produced with CIGALE with the three attenuation laws.

proved version of the older [Draine & Li \(2007\)](#) model by varying dust opacity across the radius of a galaxy. This IR model was successful in reproducing dust emissions of millions of *Herschel*-detected galaxies as a part of the HELP project ([Małek et al. 2018](#)).

3.2.5. Synchrotron emission

The VLA detection at 3 GHz of Astarte and Adonis allow us to model the synchrotron emission of our objects, taking into account a non-thermal power law of the synchrotron spectrum and the ratio of the FIR/radio correlation. The different parameters used to build our SEDs are shown in Table 3.

3.2.6. SED fitting results

In the case of Astarte, CF00 and LF17 attenuation laws result in best SED fits over C00. The BIC of every model was calculated and is shown in Table 4 along with the other quality of fit assessments. $\Delta BIC_{(C00,CF00)} = 21.88$ and $\Delta BIC_{(CF00,LF17)} = 2.29$, this privileged the best fit produced with LF17 attenuation law and therefore was taken into account in deriving the physical properties. Despite the uncertainties on any assumed SFH model, the adopted SFH here fitted the short wavelength data the best.

For the less-massive Adonis, CF00 gave overall better fits than C00 and LF17, with $\Delta BIC_{(LF17,CF00)} = 3.48$ and $\Delta BIC_{(C00,CF00)} = 5.77$. The best SED of Astarte and Adonis are shown in Figure 4. The signature of dust attenuation is clear in the two SEDs, where the heavily dust-obscured Astarte has more attenuation of its overall stellar mass than it is the case with Adonis. The derived properties of both galaxies are shown in Table 5. The L_{IR} of Astarte of the order of 10^{12} , qualifies it to be an Ultra Luminous IR Galaxy (hereafter ULIRG). While Adonis’s poor dust content is manifested in the weaker IR luminosity and lower dust mass.

To closely inspect the visible dissociation of the gas and the stellar population in Astarte, we follow the method used in [Buat et al. \(2019\)](#) by dissecting the stellar continuum and the IR emission apart and comparing their derived properties with the ones obtained using full SEDs. Taking into account the UV-NIR data ($0.3 - 8 \mu\text{m}$), the best fit for the stellar continuum was obtained with the C00 law, with $\Delta BIC_{(CF00,C00)} = 8.3$ and $\Delta BIC_{(LF17,C00)} = 2.7$. The better quality fit of the stellar continuum produced using C00 is expected, since this power-law effectively attenuates the young stellar population, while the other two laws can be equally efficient in attenuating the older stars, a behavior that translates into a rise in the near IR absorbed light and therefore a rise in the total IR emission. The IR luminosity derived from the stellar continuum gives $L_{dust} = (2.43 \pm 1.01) \times 10^{12} L_{\odot}$, relatively close to L_{dust} derived from

Physical property	Astarte	Adonis
redshift	$z_{CO} = 2.154$	$z_{spec} = 2.140$
L_{IR} ($10^{12} L_{\odot}$)	3.16 ± 0.06	0.62 ± 0.04
SFR (M_{\odot}/yr)	395 ± 20	129 ± 59
M_{\star} (M_{\odot})	$(3.74 \pm 0.19) \times 10^{11}$	$(9.37 \pm 1.76) \times 10^9$
M_{dust} ($10^9 M_{\odot}$)	1.01 ± 0.11	0.86 ± 0.13

Table 5. Summary of the physical properties obtained for Astarte and Adonis obtained with CIGALE.

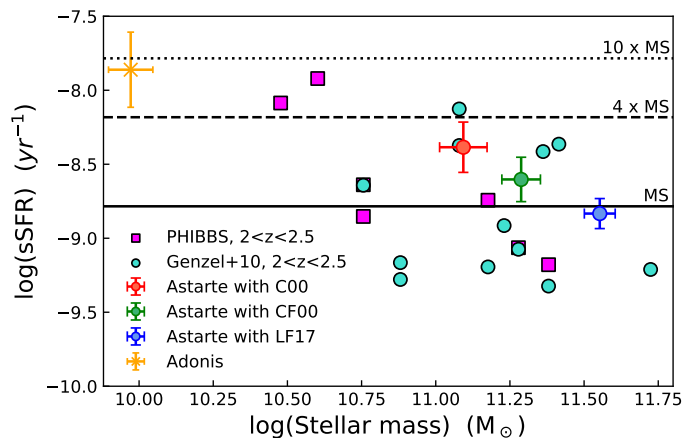


Fig. 5. Relative position of the sSFR (SFR/M_{\star}) and stellar mass of Astarte using the three attenuation laws to the main sequence of [Schreiber et al. \(2015\)](#) at $z=2$. The yellow star shows the relative position of Adonis to the MS. Magenta squares denote PHIBSS CO-detected SFGs at $z \approx 2$ ([Tacconi et al. 2013](#)). Turquoise circles are ULIRGs at $2 < z < 2.5$ from [Genzel et al. \(2010\)](#). The solid line shows the MS of [Schreiber et al. \(2015\)](#). The dashed and dotted lines are $MS \times 4$ and $MS \times 10$ respectively.

the full SED. The stellar mass derived from the stellar emission gives $(1.3 \pm 0.2) \times 10^{11} M_{\odot}$ and the $\text{SFR}_{(UV-NIR)} = 430 M_{\odot} \text{yr}^{-1}$. From the IR data (MIPS - ALMA continua), we get $L_{dust} = (3.25 \pm 0.08) \times 10^{12} L_{\odot}$, consistent with the one derived with the full SED. This result is in agreement with the results of [Buat et al. \(2019\)](#) where they found consistent dust luminosities derived from both the full SED and the IR data, while L_{dust} deduced from the stellar continuum was underestimated.

4. Discussion

Figure 5 shows the relative position of our galaxies to the MS of [Schreiber et al. \(2015\)](#). Adonis lies on $10 \times MS$ qualifying it to be a strong starburst, despite its relatively low SFR. While being a starburst, this type of source cannot be detected even by the deepest 3 mm ALMA survey (expected flux of $7 \mu\text{Jy}$), which have a $1-\sigma$ noise of $9.7 \mu\text{Jy}$ ([González-López et al. \(2020\)](#)).

Astarte is a MS galaxy with all the different attenuation recipes used. However, there is a clear difference concerning the position of Astarte relative to the MS as a result of the three attenuation laws. This is attributed to the significant difference in the derived stellar masses, with CF00 and LF17 attenuation laws resulting in larger stellar mass than C00 due to the highest attenuation in NIR. This contributes to a lower specific SFR ($\text{sSFR} = \text{SFR}/M_{\star}$) since SFRs do not differ significantly with the three laws.

Host halo masses of such $z \approx 2$ *Herschel*-detected massive MS galaxies were investigated in [Béthermin et al. \(2014\)](#) using clus-

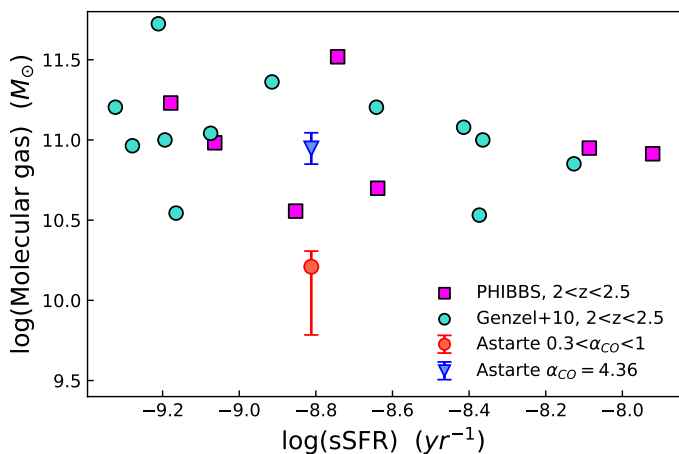


Fig. 6. Molecular gas masses derived with the CO conversion factor versus the sSFR. The magenta squares are from T13. Turquoise circles are ULIRGs at $2 < z < 2.5$ from G10. The red circle shows the position of Astarte with the used $\alpha_{CO} = 0.8$, and the associated error bar shows the variation of the molecular gas mass using $0.3 < \alpha_{CO} < 1$. The blue triangle shows the molecular gas of Astarte for a galactic CO conversion factor of 4.36.

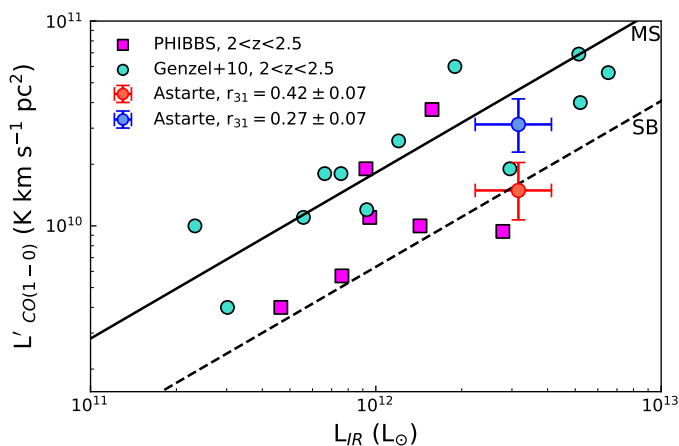


Fig. 7. Correlation between CO(1-0) luminosities and the total IR luminosity. The magenta-filled squares are from T13 and turquoise-filled circles are the sources from G10. The solid black line is the linear regression for MS galaxies (Sargent et al. 2014) and the dashed line is that for SBs (the regression lines are from the complete sample in Sargent et al. 2014).

tering and X-ray stacking and were found to reside in halos of $> 10^{13} M_{\odot}$. Such halo masses are also expected from the stellar mass to halo mass relation (Behroozi et al. 2013; Durkalec et al. 2018; Behroozi et al. 2019). Astarte is ~ 4 times less massive than the average central galaxies at $z \sim 1$ of Hilton et al. (2013) and van der Burg et al. (2013), which indicates that such MS giant galaxies continue to grow either through in situ star formation or accretion of other galaxies through the cosmic time until lower redshifts.

We compare Astarte with CO-detected samples of the same redshift range from Genzel et al. (2010) (labeled G10) and Tacconi et al. (2013) (labeled T13). These samples of SFGs have constrained CO detections, and well-investigated physical parameters (in Sargent et al. 2014).

We compare the molecular gas mass of Astarte derived from the CO emission line with that of G10 and T13 galaxies in

Figure 6. G10 uses a galactic conversion factor for SFGs and $\alpha_{CO} = 1$ for ULIRGs, while T13 adopts a galactic conversion factor for all their sources. Our choice of $\alpha_{CO} = 0.8$ underestimates the molecular gas mass of Astarte than the galaxies of G10 and T13. However, $\alpha_{CO} = 4.36$ produces a higher molecular gas mass with respect to its sSFR.

In Figure 7 we show the correlation between CO luminosities and the total infrared luminosities. IR luminosities were derived from the SFRs of all the sources (G10, T13 and Astarte) using the Kennicutt relation (Kennicutt 1998). The initial choice of $r_{31} = 0.42 \pm 0.07$ (the average in Daddi et al. 2015) places Astarte on the SB line from Sargent et al. (2014), contradicting its SED result. We therefore investigate the lowest excitation ratio from Daddi et al. (2015) of $r_{31} = 0.27 \pm 0.07$. This lower ratio moves Astarte closer to the MS within the error bars.

Using the total molecular gas mass of Astarte derived with the least excited CO(3-2) from Daddi et al. (2015) ($r_{31} = 0.27 \pm 0.07$), and assuming a galactic conversion factor, we estimate the gas fraction $f_{gas} = M_{gas}/(M_{gas} + M_{\star}) = (0.27 \pm 0.07)$. Although this falls within the lower limits of typical molecular gas fractions found in SFGs at $z \sim 2$ in Santini et al. (2014) and Béthermin et al. (2015), an α_{CO} adapted for SB with a higher r_{31} ratio reduces the gas fraction significantly.

The gas mass derived with a galactic conversion factor gives Astarte a rather small depletion time of 0.22 ± 0.07 Gyrs, making it very efficient at forming stars (for comparison, SBs have a depletion time of the order of ~ 100 Myrs, (see Fig. 10 in Béthermin et al. 2015)). Recently, Elbaz et al. (2018) found that compact SFGs on the MS with a relatively low depletion time are not uncommon. These active ultra-massive objects can be hidden at the higher end of the tail of the MS. The average depletion time for Elbaz et al. (2018) galaxies is around 0.25 Gyrs, and although we do not detect the continuum of Astarte with ALMA, its CO emission is compact as it is the case for the continuum of ALMA-detected galaxies from Elbaz et al. (2018). This is also confirmed in Puglisi et al. (2019) where compact massive galaxies at the top of the MS exhibit high SFRs at their cores following their SB epoch.

5. Conclusion

In this paper, we analyzed two galaxies, Astarte and Adonis, at the peak of the SFR density using multiwavelength dissection combining ALMA observations with UV-submm SED modeling. We investigated the molecular gas content of Astarte through the ALMA detection of its CO(3-2) emission, relying on different excitation ratios of $L'_{CO(3-2)}/L'_{CO(1-0)}$ and different CO conversion factors. A galactic conversion factor when used along with the least excitation ratio from Daddi et al. (2015) confirmed the relative position of Astarte to the MS, as found from its SED modeling. Although the obtained gas fraction is on the lower limits of that in MS galaxies (Santini et al. 2014; Béthermin et al. 2015), a possible explanation might be that the CO(3-2) instantaneous emission does not fully recover the molecular mass and the dynamics of Astarte, due to its weak excitation (Daddi et al. 2015). Detections of other transition levels of CO would be helpful to better constrain the molecular mass of Astarte, and therefore its physical characteristics.

The physical dissociation of the CO line and the rest-frame stellar population in Astarte was also investigated as done in Buat et al. (2019), by deriving physical properties from the stellar emission (UV-NIR) and the IR emission apart. As in Buat

et al. (2019), the dust luminosity derived from the full SED is in agreement with the one derived from the IR emission, while L_{dust} derived from the stellar emission is slightly underestimated. Furthermore, C00 attenuation law was preferred when fitting the stellar continuum only. This is consistent with the results of Buat et al. (2019) for galaxies with the same radii extension of rest-frame stellar emission and ALMA-detected emission. LF17 attenuation law, which was tuned for ULIRGs at $z \sim 2$ succeeds the most in mimicking the dust attenuation of Astarte when fitting the whole UV-submm SED, this however results in higher stellar mass.

The molecular mass of Astarte, obtained with a galactic conversion factor and the lowest excitation ratio from Daddi et al. (2015), contributes to ~ 0.9 of its total dynamical mass, which is a larger contribution than what is found in ULIRGs of Neri et al. (2003). SFRs and stellar masses derived from the SED fittings show that Adonis is a SB galaxy, while Astarte is on the MS of SFGs. However, the small gas fraction makes Astarte very efficient in forming stars, whose depletion time is an order of magnitude lower than what is expected in typical MS galaxies (B  thermin et al. 2015). This SB-like star formation activity on the MS was found for massive compact SFGs in Puglisi et al. (2019), in their post-SB phase. Low depletion times of MS massive galaxies were also found in Elbaz et al. (2018), confirming that Astarte is caught in the middle of quenching following an earlier SB activity.

Central galaxies at $z \sim 1$ from Hilton et al. (2013) and van der Burg et al. (2013) are ~ 4 times more massive than Astarte. This indicates that even massive objects that are on the high-end of the MS, when the Universe was undergoing its peak in the star formation rate density, continue their mass assembly down to lower redshift.

Acknowledgements. M.H. and K.M. have been supported by the National Science Centre (UMO-2018/30/E/ST9/00082). We acknowledge and thank the referee for a thorough and constructive report, which helped improving this work. This paper makes use of the following ALMA data: ADS/JAO.ALMA#2013.1.00914.S. ALMA is a partnership of ESO (representing its member states), NSF (USA) and NINS (Japan), together with NRC (Canada), MOST and ASIAA (Taiwan), and KASI (Republic of Korea), in cooperation with the Republic of Chile. The Joint ALMA Observatory is operated by ESO, AUI/NRAO and NAOJ.

References

Alonso, M. S., Tissera, P. B., Coldwell, G., & Lambas, D. G. 2004, MNRAS, 352, 1081

Arnouts, S. & Ilbert, O. 2011, LePHARE: Photometric Analysis for Redshift Estimate (ascl:1108.009)

Behroozi, P., Wechsler, R. H., Hearin, A. P., & Conroy, C. 2019, MNRAS, 488, 3143

Behroozi, P. S., Wechsler, R. H., & Conroy, C. 2013, ApJ, 770, 57

B  thermin, M., Daddi, E., Magdis, G., et al. 2015, A&A, 573, A113

B  thermin, M., Fudamoto, Y., Ginolfi, M., et al. 2020, A&A, 643, A2

B  thermin, M., Kilbinger, M., Daddi, E., et al. 2014, A&A, 567, A103

B  thermin, M., Wu, H.-Y., Lagache, G., et al. 2017, A&A, 607, A89

Blain, A. W., Smail, I., Ivison, R. J., Kneib, J. P., & Frayer, D. T. 2002, Phys. Rep., 369, 111

Bolatto, A. D., Wolfire, M., & Leroy, A. K. 2013, ARA&A, 51, 207

Boquien, M., Burgarella, D., Roehlly, Y., et al. 2019, A&A, 622, A103

Bothwell, M. S., Aguirre, J. E., Chapman, S. C., et al. 2013a, ApJ, 779, 67

Bothwell, M. S., Smail, I., Chapman, S. C., et al. 2013b, MNRAS, 429, 3047

Bourne, N., Dunlop, J. S., Merlin, E., et al. 2017, MNRAS, 467, 1360

Bruzual, G. & Charlot, S. 2003, MNRAS, 344, 1000

Buat, V., Boquien, M., Ma  lek, K., et al. 2018, A&A, 619, A135

Buat, V., Ciesla, L., Boquien, M., Ma  lek, K., & Burgarella, D. 2019, A&A, 632, A79

Buat, V., Heinis, S., Boquien, M., et al. 2014, A&A, 561, A39

Burgarella, D., Buat, V., & Iglesias-P  ramo, J. 2005, MNRAS, 360, 1413

Calzetti, D., Armus, L., Bohlin, R. C., et al. 2000, ApJ, 533, 682

Carilli, C. L. & Walter, F. 2013, ARA&A, 51, 105

Casey, C. M., Scoville, N. Z., Sanders, D. B., et al. 2014, ApJ, 796, 95

Cassata, P., Morselli, L., Faisst, A., et al. 2020, A&A, 643, A6

Cattaneo, A., Faber, S. M., Binney, J., et al. 2009, Nature, 460, 213

Chabrier, G. 2003, PASP, 115, 763

Chapman, S. C., Blain, A. W., Ivison, R. J., & Smail, I. R. 2003, Nature, 422, 695

Chapman, S. C., Blain, A. W., Smail, I., & Ivison, R. J. 2005, ApJ, 622, 772

Charlot, S. & Fall, S. M. 2000, ApJ, 539, 718

Ciesla, L., Boquien, M., Boselli, A., et al. 2014, A&A, 565, A128

Ciesla, L., Boselli, A., Elbaz, D., et al. 2016, A&A, 585, A43

Ciesla, L., Elbaz, D., & Fensch, J. 2017, A&A, 608, A41

Ciesla, L., Elbaz, D., Schreiber, C., Daddi, E., & Wang, T. 2018, A&A, 615, A61

Coil, A. L., Newman, J. A., Croton, D., et al. 2008, ApJ, 672, 153

Combes, F. 2017, Frontiers in Astronomy and Space Sciences, 4, 10

Conroy, C. 2013, ARA&A, 51, 393

da Cunha, E., Charlot, S., & Elbaz, D. 2008, MNRAS, 388, 1595

Daddi, E., Dannerbauer, H., Liu, D., et al. 2015, A&A, 577, A46

Daddi, E., Elbaz, D., Walter, F., et al. 2010, ApJ, 714, L118

Decarli, R., Walter, F., G  nzalez-L  pez, J., et al. 2019, ApJ, 882, 138

Donevski, D., Lapi, A., Ma  lek, K., et al. 2020, A&A, 644, A144

Downes, D. & Solomon, P. M. 1998, ApJ, 507, 615

Downes, D. & Solomon, P. M. 2003, ApJ, 582, 37

Draine, B. T., Aniano, G., Krause, O., et al. 2014, ApJ, 780, 172

Draine, B. T. & Li, A. 2007, ApJ, 657, 810

Dubois, Y., Gavazzi, R., Peirani, S., & Silk, J. 2013, MNRAS, 433, 3297

Dunlop, J. S., McLure, R. J., Biggs, A. D., et al. 2017, MNRAS, 466, 861

Durkalec, A., Le F  vre, O., Pollo, A., et al. 2018, A&A, 612, A42

Elbaz, D., Leiton, R., Nagar, N., et al. 2018, A&A, 616, A110

Faisst, A. L., Schaerer, D., Lemaux, B. C., et al. 2020, ApJS, 247, 61

Genzel, R., Tacconi, L. J., Gracia-Carpio, J., et al. 2010, MNRAS, 407, 2091

Gonz  lez-L  pez, J., Novak, M., Decarli, R., et al. 2020, ApJ, 897, 91

Greve, T. R., Bertoldi, F., Smail, I., et al. 2005, MNRAS, 359, 1165

Grupponi, C., B  thermin, M., Loiacono, F., et al. 2020, A&A, 643, A8

Hainline, L. J., Blain, A. W., Smail, I., et al. 2011, ApJ, 740, 96

Hilton, M., Hasselfield, M., Sif  n, C., et al. 2013, MNRAS, 435, 3469

Hopkins, A. M. & Beacom, J. F. 2006, ApJ, 651, 142

Jin, S., Daddi, E., Liu, D., et al. 2018, ApJ, 864, 56

Kennicutt, Robert C., J. 1998, ARA&A, 36, 189

Komatsu, E., Smith, K. M., Dunkley, J., et al. 2011, ApJS, 192, 18

Laigle, C., McCracken, H. J., Ilbert, O., et al. 2016, ApJS, 224, 24

Lambas, D. G., Tissera, P. B., Alonso, M. S., & Coldwell, G. 2003, MNRAS, 346, 1189

Law, D. R., Steidel, C. C., Erb, D. K., et al. 2009, ApJ, 697, 2057

Lilly, S. J., Le Brun, V., Maier, C., et al. 2009, ApJS, 184, 218

Lo Faro, B., Buat, V., Roehlly, Y., et al. 2017, MNRAS, 472, 1372

Lutz, D., Poglitsch, A., Altieri, B., et al. 2011, A&A, 532, A90

Madau, P. & Dickinson, M. 2014, ARA&A, 52, 415

Ma  lek, K., Buat, V., Roehlly, Y., et al. 2018, A&A, 620, A50

McMullin, J. P., Waters, B., Schiebel, D., Young, W., & Golap, K. 2007, in Astronomical Society of the Pacific Conference Series, Vol. 376, Astronomical Data Analysis Software and Systems XVI, ed. R. A. Shaw, F. Hill, & D. J. Bell, 127

Mendez, A. J., Coil, A. L., Lotz, J., et al. 2011, ApJ, 736, 110

Merlin, E., Fontana, A., Castellano, M., et al. 2018, MNRAS, 473, 2098

Micha  owski, M. J., Dunlop, J. S., Cirasuolo, M., et al. 2012, A&A, 541, A85

Murphy, E. J., Chary, R. R., Dickinson, M., et al. 2011, ApJ, 732, 126

Neri, R., Genzel, R., Ivison, R. J., et al. 2003, ApJ, 597, L113

Noeske, K. G., Weiner, B. J., Faber, S. M., et al. 2007, ApJ, 660, L43

Noll, S., Burgarella, D., Giovannoli, E., et al. 2009, A&A, 507, 1793

Oliver, S. J., Bock, J., Altieri, B., et al. 2012, MNRAS, 424, 1614

Puglisi, A., Daddi, E., Liu, D., et al. 2019, ApJ, 877, L23

Riechers, D. A., Boogaard, L. A., Decarli, R., et al. 2020, ApJ, 896, L21

Rodighiero, G., Daddi, E., Baronchelli, I., et al. 2011, ApJ, 739, L40

Salim, S. & Narayanan, D. 2020, ARA&A, 58, 529

Santini, P., Maiolino, R., Magnelli, B., et al. 2014, A&A, 562, A30

Sargent, M. T., Daddi, E., B  thermin, M., et al. 2014, ApJ, 793, 19

Schmidt, M. 1959, ApJ, 129, 243

Schreiber, C., Glazebrook, K., Nanayakkara, T., et al. 2018a, A&A, 618, A85

Schreiber, C., Labb  , I., Glazebrook, K., et al. 2018b, A&A, 611, A22

Schreiber, C., Pannella, M., Elbaz, D., et al. 2015, A&A, 575, A74

Smail, I., Ivison, R. J., & Blain, A. W. 1997, ApJ, 490, L5

Smol  i  , V., Novak, M., Bondi, M., et al. 2017, A&A, 602, A1

Solomon, P. M., Downes, D., Radford, S. J. E., & Barrett, J. W. 1997, ApJ, 478, 144

Tacconi, L. J., Neri, R., Chapman, S. C., et al. 2006, ApJ, 640, 228

Tacconi, L. J., Neri, R., Genzel, R., et al. 2013, ApJ, 768, 74

Takeuchi, T. T., Buat, V., & Burgarella, D. 2005, A&A, 440, L17

van der Burg, R. F. J., Muzzin, A., Hoekstra, H., et al. 2013, A&A, 557, A15

Wang, T., Schreiber, C., Elbaz, D., et al. 2019, Nature, 572, 211

We  b, A., De Breuck, C., Marrone, D. P., et al. 2013a, ApJ, 767, 88

We  b, A., De Breuck, C., Vieira, J. D., et al. 2013b, in Astronomical Society of the Pacific Conference Series, Vol. 476, New Trends in Radio Astronomy in the ALMA Era: The 30th Anniversary of Nobeyama Radio Observatory, ed. R. Kawabe, N. Kuno, & S. Yamamoto, 33

Whitaker, K. E., Pope, A., Cybulski, R., et al. 2017, ApJ, 850, 208

Wild, V., Charlot, S., Brinchmann, J., et al. 2011, MNRAS, 417, 1760